

International Journal of Signal and Imaging Systems Engineering

ISSN online: 1748-0701 - ISSN print: 1748-0698
<https://www.inderscience.com/ijwise>

Image correlation, non-uniformly sampled rotation displacement measurement estimation

Nicholas Wells, Chung W. See

DOI: [10.1504/IJSISE.2023.10059439](https://doi.org/10.1504/IJSISE.2023.10059439)

Article History:

Received:	23 November 2021
Last revised:	01 June 2022
Accepted:	01 August 2022
Published online:	28 September 2023

Image correlation, non-uniformly sampled rotation displacement measurement estimation

Nicholas Wells*

Metrix NDT Limited, Aerodrome Close,
Loughborough, LE11 5RJ, UK
Email: nwells_nottingham1@yahoo.com
*Corresponding author

Chung W. See

Faculty of Engineering,
University of Nottingham,
University Park, Nottingham, NG7 2RD, UK
Email: cwsphonyacc@talktalk.net

Abstract: A rotation invariant image correlation algorithm is described which measures and locates the rotational error of individual spatial frequency components. This information may then be interpreted to track signal dependent signatures, analyse spatial frequencies with much higher bandwidths and form optimal matched and generalised correlation filters. The technique is based on image re-sampling and a non-uniform sampling interval that is adjusted depending on its distance from the origin of the polar map. A nearest-neighbour polar interpolated grid scheme, comparable to linear interpolation error, achieves accuracies of 0.1% of a degree. Preliminary measurements based on images containing natural and rigid structure are presented. The algorithm also has potential applications for data-driven image registration and deformation analysis with small variations.

Keywords: image transforms; image analysis; correlation filters; rotation displacement measurement.

Reference to this paper should be made as follows: Wells, N. and See, C.W. (2023) 'Image correlation, non-uniformly sampled rotation displacement measurement estimation', *Int. J. Signal and Imaging Systems Engineering*, Vol. 12, No. 4, pp.148–157.

Biographical notes: Nicholas Wells obtained his MEng and PhD degree in electrical electronic engineering at the University of Nottingham. He then joined MetrixNDT Limited Loughborough, where he develops X-ray imaging systems. His current research focuses on developing data-driven signal and image processing techniques with application to high sensitivity NDT systems.

Chung W. See obtained his undergraduate and PhD degree, both from the University College London. After two years of post-doctoral experience, he moved to Rank Taylor Hobson Limited Leicester, as a Senior Research Engineer, where he developed optical based non-contact metrology equipment. He then joined the Department of Electrical and Electronic Engineering, University of Nottingham as a Lecturer and then became an Associate Professor. Apart from giving lectures to undergraduate and postgraduate courses, he conducted research, concentrating on high sensitivity and high resolution imaging systems, with application, among others, in biological sciences. CWS has retired since January 2019.

1 Introduction

Digital Image Correlation (DIC) is a non-contact method to accurately track and measure deformation between images. Important in many science and engineering applications, acquiring 2D/3D representations of a samples surface opens up DIC to new and complex investigations. In this paper we report our initial findings for a novel sampling and interpolation technique to obtain high accuracy 2D rotation

displacement measurements and a signal dependent matched filter. The technique is demonstrated using the structural content of single image frames potentially useful for data driven image understanding and analysis.

A non-uniformly sampled correlation grid samples an image frame several times with different sampling densities and has distinct advantages over uniformly sampled grids. The presented technique locates and measures accurate rotation displacement errors, which ordinarily, for

uniformly sampled grids diminish the usable spatial bandwidth of signals. In addition newly sampled (re-sampled) functions offer adaptable filtering usages. Rotational displacement measurements, which are strongly affected by different sampling densities, can be obtained using combined feature descriptors and extractors such as speeded up robust features (SURF) (Bay et al., 2008), binary robust invariant scalable key-points (BRISK) (Leutenegger et al., 2011) and orientated brief and rotated fast (ORB) (Rublee et al., 2011). These techniques inspect for pixel connectivity and local statistics in image regions over scales using blob and corner detection. In a Cartesian coordinate system, image features may be recovered by detecting directional variations in x and y planes. These features typically correspond to continuous and discontinuous edge transitions and texture (Lowe, 2003). However, after the removal or redundancy of pictorial data the remaining image information may still contain noise. In this paper we are concerned with the constraints of additive noise in imaging systems. In terms of signal-to-noise (S/N) and image correlation, the development of optimal solutions to recover salient image content, from noisy signals, may become complex. In general application, there is no guarantee that similarities between a reference and displaced signal are found from critical or discriminate visual features. Furthermore, it is implied that such features are located within a narrow or broad spatial bandwidth. Therefore, it can be more appropriate to adopt techniques that take into account the spatial correlation of signal and statistical fluctuation: perhaps of texture, edges and corners.

The proposed method in this work is aimed at applications where measurement sensitivity is a key parameter of the analysis. Therefore many of the more sophisticated algorithms may not be applicable here. One sophisticated approach is deep registration which capitalises on the success of convolutional neural networks and deep learning paradigms (Xiang et al., 2021; Villena-Martinez et al., 2021) to detect key points between sets of images. This feature based approach is much like the application of SIFT in formulating a combined feature extractor/descriptor but with improved speed and identification of salient points (Lee et al., 2021). However, it remains the case that approaches in image registration following a deep learning methodology lack reliability and accuracy (Villena-Martinez et al., 2021). Two reasons for this are: firstly, the difficulty in acquiring the quantity and quality of a training data set required in deep learning to generalise variation. Secondly, the development of appropriate methods that validates the outcomes of the high level abstract processing of deep learning layers. It therefore remains desirable to use area based methods as a standalone approach and to incorporate as traditional computer vision methods into (deep) machine learning models (O'Mahony et al., 2019); with the aim of improving accuracy and speed, and to help drive innovation. A key advantage of Fourier based (area) techniques over feature based methods, such as SURF or ORB, are their theoretical accuracy. Of which,

discrete Fourier transform based techniques (Tong et al., 2019) remain a highly focused study of research (Reddy and Chatterji, 1996; Wolberg and Zokai, 2000; Sarvaiya et al., 2012; Casasent and Psaltis, 1976) for their application in image registration problems (Rasmy et al., 2021). Optically demonstrated in Casasent and Psaltis (1976), one such method named the Fourier-Mellin transform seeks to recover translation, rotation and scale using a log-polar transformation. However, the recoverable rotation and scale measurement range of this method are self-limiting. This is due to a non-standard coordinate transform, a distortion of the signal spectrum due to scale changes and removal of the phase spectrum to achieve small translation invariance. Furthermore, using the Fourier transform, it is only translation and rotational shifts that are mutual since scale is isolated using the log-polar transformed 1D Mellin-transform. In addition, due to sampling issues, the location of spatial signal components are often assumed and high S/N components may be intentionally or unintentionally filtered out. In the Fourier domain, limitations are also imposed by including scale invariance and selecting image content to estimate *a priori*. Ultimately, this can restrict the measurement and application range of pattern inspection techniques. Even so, DIC is heavily adopted in measurement science, particularly for applications involving non-destructive evaluation (Sousa et al., 2018; Charret and Tatam, 2019). Improvements in algorithm efficiency, measurement sensitivity and operating range are key drivers in developing DIC techniques. For technologies with increased demand for high resolution rotation measurements (Schreier et al., 2009), post-process optimisation is as equally important as, configuring hardware to measurement resolution criteria. Critically, spatial correlations are required to be least sensitive to the effect of hardware and environmental factors (such as device calibration and image recording) that introduce and accumulate measurement errors into a system (Titkov and Panin, 2019).

This study focuses on the implications of under-sampling to speed up calculations and oversampling to improve accuracy. We describe an image correlation technique which has the advantage of simultaneously providing a high accuracy rotation displacement measurement and a signal dependent matched filter. Furthermore, a subset or block of spatial frequencies can be selected to generalise an optimum filter: such as bandpass or bandstop responses and cascaded implementation. Our technique combines up-sampling, which decreases the sampling interval in the spatial domain, and a non-uniform sampling interval that is adjusted depending on its distance from the origin (centre) of the polar map. By adopting this approach, spatial frequencies can be measured and analysed using much higher bandwidths than that can be ordinarily and efficiently obtained using uniformly sampled grids.

In order to achieve this, an image and a rotated copy of the image are first re-sampled with a higher sampling density. To improve the accuracy of the tracked peak location errors that may have been distorted by rotation displacements; the correlation peak is modelled using a

second-order polynomial (Kumar et al., 1992). A second order model is adopted since the correlations shape is a parabola.

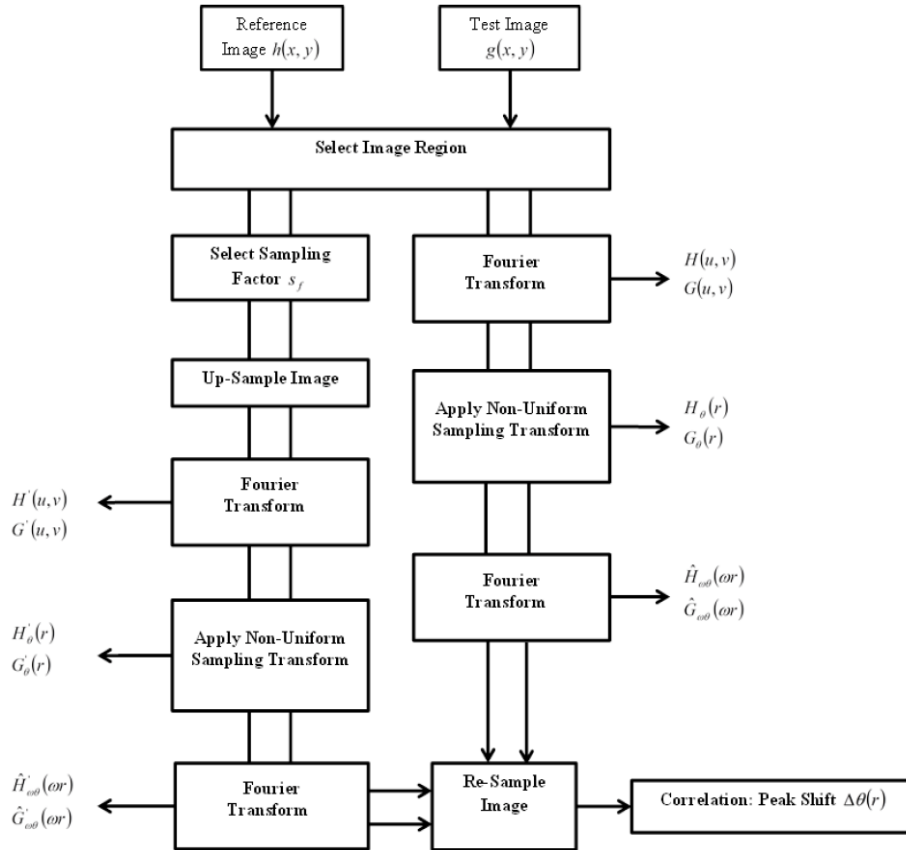
Firstly, in Sections 2 and 3, the principal behind this technique and a description of its implementation are presented. Initial results obtained with this method are discussed in Section 4 to demonstrate the ability of the technique to measure small rotational variation and form signal dependent filters. Finally, we will compare these measurements with region-based methods in Section 5 and discuss briefly alternative implementations to improve measurement accuracy.

2 Non-uniformly sampled rotation displacement measurement

As outlined in the introduction, our technique simultaneously obtains high accuracy broad spatial bandwidth measurements and a signal dependent matched filter. In order to achieve this, an image is copied to form a reference and test image. These images are both resampled with a higher sampling density to resolve the peak shift of the correlated signal. The principle of the correlation algorithm can be best described with reference to the diagram in Figure 1 and the appendix which derives the necessary understanding of the mathematical techniques involved.

For an image $h(x,y)$ it may be desirable due to the application to select regions of an image containing higher densities of information. On the assumption that the data signal is finite and periodic a rectangular window can be applied prior to obtaining the images Fourier transform $H(u,v)$; to minimise the undesirable effect of spectral leakage a Hann window, for example, can be applied. To improve the accuracy of the correlation measurement at the original image resolution, a sampling factor s_f specified by an integer value, up-samples the image data in the spatial domain. This is achieved by zero padding the image by a constant determined by s_f . A sampling mechanism is then applied to both $H(u,v)$ and $H'(u,v)$ to determine a non-uniformly sampled polar spatial map of the image at the original and resampled sampling densities. The theory of operation of this mechanism is outlined in Section 3. The Fourier transform of the non-uniformly sampled signals, $\hat{H}_{\omega\theta}(\omega r)$ and $\hat{H}'_{\omega\theta}(\omega r)$, creates a look up table containing re-sampled polar spatial frequencies. The polar spatial frequency values at the polar grid locations of the original sampling density are replaced with those higher sampled values. This (reference) signal is input into the correlation function. The test signal $g(x,y)$ is obtained by copying $h(x,y)$ and prepared in the same way as $h(x,y)$. Whereby, an image section may be selected and a window function subsequently applied.

Figure 1 Overview of the rotation invariant correlation algorithm



The equivalent functions generated from the test image $g(x, y)$ are: the Fourier transforms of the original and up-sampled image $G(u, v)$ and $G'(u, v)$; the Fourier transforms of the non-uniformly sampled original and up-sampled test signals: $\hat{G}_{\omega\theta}(\omega r)$ and $\hat{G}'_{\omega\theta}(\omega r)$. Finally, the modified test signal is input into the correlation function. The location of the correlation peak is then resolved to determine the amount of rotational shift $\Delta\theta(r)$ in each radial component.

3 Theory

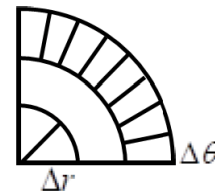
Measurements are fundamentally limited by the technical parameters of an imaging system. For example, in X-ray systems, the penumbra is determined by imaging geometry and X-ray source focal spot diameter. However, improvements in accuracy can be approximated by interpolating between discretely sampled points. As mentioned in the previous section a sampling mechanism is applied to the Fourier transformed image. The purpose of this step is to accurately map between angular and Cartesian grid points. Before we explore the theory of this transformation, it is important to consider the effects of uniform sampling in image correlation. Variations in x and y at low and high image spatial frequencies may correspond to shape and edge transitions in the spatial domain. If edge features are focused on, a large proportion of the spatial bandwidth will be removed from the analysis of the image. Conversely, if shape or slower variations are focused on other and potentially interesting spatial components will be removed. The implication of this on correlation performance is that a correlation signal is bound to a broad or narrow range of spatial frequencies that a chosen image feature occupies. Furthermore, it may be necessary for applications to consider all spatial frequencies, in particular, features distorted by low frequency variation. To measure a shift in translation, the sampling condition of the Fourier transform is trivially met. This is because the spacing between all spatial frequencies is distributed uniformly over a Cartesian grid. Therefore, a broad or narrow range of spatial frequencies can be accurately sampled by the correlation.

If a data set is arranged on a polar coordinate grid, uniform sampling will restrict the measurement range, accuracy and precision of the correlation. If image features are carefully chosen, sampling on a polar grid can be adjusted to adequately sample the spatial bandwidth occupied by that feature. However, this may restrict the signal content chosen for the correlation since measurement accuracy will be set by the location of a sampled point. The precision and accuracy of a correlation signal will be affected by under-sampling and oversampling in the polar domain. Therefore, recovery of the correlation peak location will determine the precision of a correlation measurement. Moreover, correct alignment between angular and Cartesian grid point's in-between $\pi/4$ intervals will improve correlation measurement precision.

When dealing with grid alignment error using a set of sampled data, the resolution in determining a shift of a function is limited to $\pm\Delta/2$ with Δ being the sampling interval. The quantity $\Delta/2$ can therefore be regarded as the upper limit of error. Assuming the original set of data satisfies the sampling criterion; this error can be removed by convolving the correlation signal with a sinc function. A non-favourable consequence of sinc interpolation is that every discrete point of the signal is operated on to reconstruct the signal. Hence, computation time increases proportionally. Approximations to the sinc convolution are made by determining the nearest neighbour value and calculating linear and cubic polynomials. Except for nearest-neighbour, the S/N of the signal interpolator increases as the neighbourhood sample size increases. In many applications, nearest-neighbour interpolation does not provide sufficient accuracy but can be improved by utilising properties of non-uniformly sampled polar grid intervals. In Section 4 we present examples of this sampling mechanism at work.

In a polar coordinate system, satisfying the sampling condition becomes non-trivial since the sampling density over any area will be dependent on its distance from the origin of the polar map. An additional point to consider is that using higher-order polynomials may increase the S/N but not measurement accuracy. As previously stated, under-sampling on the polar grid can lead to aliasing and poor precision in locating the correlation peak; whereas oversampling will improve the precision. To ensure that the sampling condition is met for each radial component, the correlation is reduced to a series of 1D correlations' between $G_\theta(r)$ and $H_\theta(r)$. This coordinate transformation is best described with reference to Figure 2. The radial interval Δr is fixed over the entire polar map and the angular interval $\Delta\theta$ decreases as the sampling point moves further away from the center (origin). The lower and upper bound conditions are redefined as $\Delta\theta_{r(1)} = 2\pi r_1 / s_{rate} \leq 1$ and $\Delta\theta_{r(max)} = 2\pi r_{max} / s_{rate} r_{max} \leq 1$, where s_{rate} denotes the sampling rate. The aim of this 1D non-uniform coordinate transformation is to maintain the same arc length, $r\Delta\theta$, on the whole grid by linearly increasing s_{rate} .

Figure 2 Non-uniform polar sampling



Whereas, additional grid point locations are linearly proportional to the re-sampling factor s_f . The interpolation accuracy relies on the number of points to sample a grid

location. To obtain a higher sampled source image each radial component at locations r_j , over the entire original signal boundary are re-sampled according to $r_j = v_j / s_f$, for $j=0:(v/2)-1$. Finally, the polar spatial frequency components are input to the correlation. Since we are interested in the full spatial bandwidth of the image, the correlation can be written as

$$C_\theta(r) = \frac{\bar{H}_\theta(r)\bar{G}_\theta^*(r)}{\langle\langle\|\bar{H}_\theta(r)\|,\|\bar{G}_\theta(r)\|\rangle\rangle}. \quad (1)$$

We have replaced $\hat{G}_\theta(r)$ and $\hat{H}_\theta(r)$ notation in Equation (1) with the mean adjusted functions $\bar{G}_\theta(r)$ and $\bar{H}_\theta(r)$. In addition to the broad spatial bandwidth range of the correlation in equation (1), shape features particular to the image input to the correlation can also be parameterised. In contrast to phase correlation, to determine a rotational (and translational) shift, low frequency information is lost. Furthermore only narrow spatial bandwidths can be correlated.

The computational complexity of the proposed technique is bound by the geometric term $\sum_{j=0}^{r-1} r_j s_{rate}$ whose asymptotic value is determined based on the number of sampling points in each 1D correlation between a reference and target. Using big O notation, first consider that for an $M \times N$ image transformed to a polar grid, the sampling density $N_{\omega\theta}$ at each radial component linearly increases as the radial index increments away from the centre of the polar grid. The increase of each radii sampling density is proportional to the sampling rate (s_{rate}). Based on this understanding, the complexities of the dominant terms in the proposed method are

$$\phi_{max} \left[MN(\log(M) + \log(N)) + \theta_{max}(MN(\log(M) + \log(N))) \right. \\ \left. + r_{max}(2(N_{\omega\theta}(\log(N_{\omega\theta}))) + N_{\omega\theta}^2) \right].$$

For one correlation between a rotating reference and rotating target, where the respective rotation in ϕ and θ are set to 1, the complexity reduces to

$$2(MN(\log(M) + \log(N))) + r_{max}(2(N_{\omega\theta}(\log(N_{\omega\theta}))) + N_{\omega\theta}^2).$$

The fastest growing function in the algorithms complexity is $N_{\omega\theta}^2$, this is proportional to the asymptotic value of the geometric sum $\sum_{j=0}^{r-1} r_j s_{rate}$. This complexity then scales

linearly according to the number of rotations or scans in ϕ and θ . One method to reduce the complexities scale is to incorporate data driven procedures to identify *apriori* of rotational patterns to restrict the range of ϕ and θ . The time at which a computers cpu can perform this calculation is determined by computer hardware, programming language and compiler. Hardware acceleration may also be considered by using a gpu.

4 Results

In this section we describe the preliminary results obtained from the correlation technique. We compare five images, three containing typical natural structures and two containing typical rigid structures. The purpose of testing the technique on different image content is to see how image patterns may influence overall measurement accuracies. In each presented test sample in Figure 3, the images are 470×470 pixels and the constant sampling interval, $\Delta\theta$, determined from the non-uniform sampling transformation, is 0.785° . Finally, the measurement accuracy of each correlation rotation map are compared with SURF, BRISK and ORB feature based methods.

In this discussion we are concerned with a reference and a rotated image. A rotation map is obtained by rotating $g(x, y; \theta)$ through 180° with 1° increments. These rotations are compared with $h(x, y; \varphi)$ rotated through 180° with 5° increments. We refer to the rotated test and reference images as $G(u, v; \theta_{(0,\pi)})$ and $H(u, v; \varphi_{(0,\pi)})$. Figure 4 demonstrates how the rotation error (with no up-sampling), for the test image Figure 3(a), propagates through $G(u, v; \theta_{(0,\pi)})$ and $H(u, v; \varphi_{(0,\pi)})$. We show one rotation of $H(u, v; \varphi_{(0,\pi)})$ to demonstrate the impact of nearest-neighbour interpolation error. Figure 4(a)–(d) presents the tracked errors $\sigma_{\theta(r)}$, for a subset of radial cut-off points: whereby, $r_j; j = 50, 75, 125, 150$. There may also be initial transient errors in the sampling transformation even though the sampling condition has been met. On this basis and for further simulation we set $j = 50$ as the initial position. In practice, this value is determined by assessing the error variation across the entire images spatial bandwidth on an image-by-image basis.

Figure 3 Test images (Deng et al., 2009), (a)–(c) contain typical natural structure and (d)–(e) contain typical rigid structure

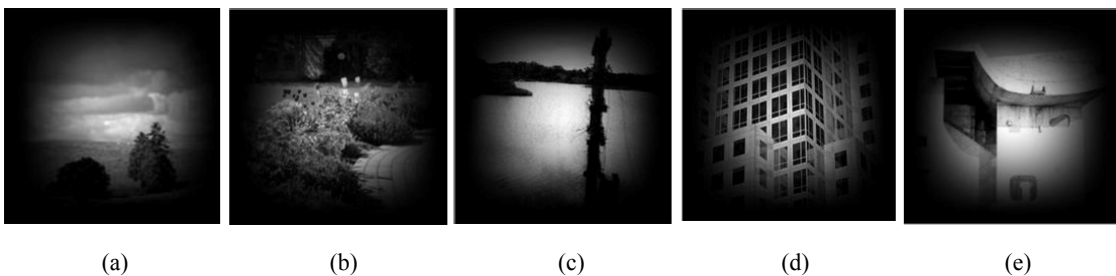
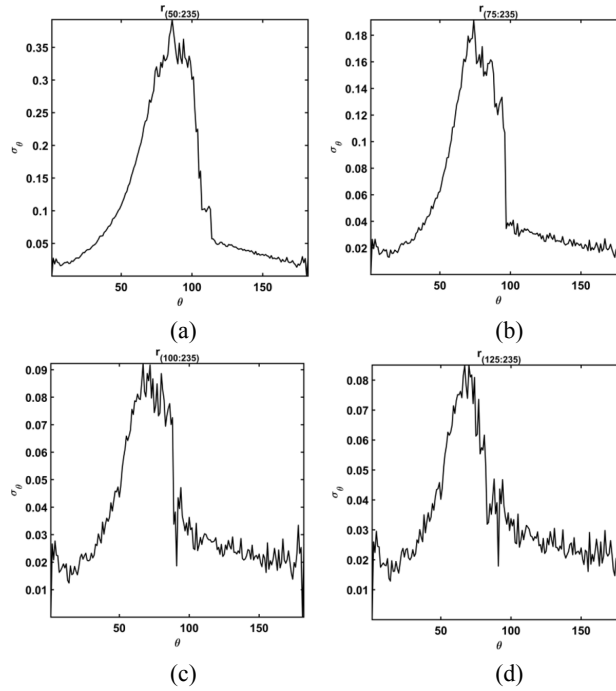


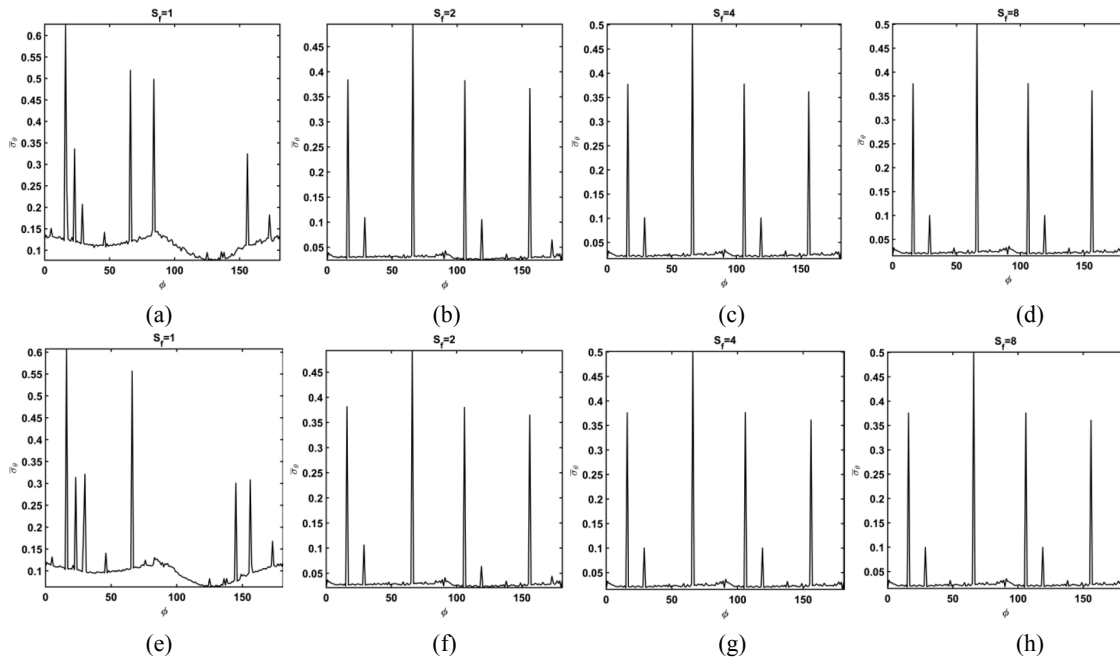
Figure 4 Correlation error propagation processes (a)–(d) standard deviation of rotation error σ_θ (y-axis) at test signal rotation angle θ (x-axis), for $r_j; j = 50, 75, 125, 150$



Clearly the measurement error, demonstrated in Figure 4(a), increases as the rotation approaches 90° . This error is systematic and due to nearest-neighbour interpolation values not discretely defined on a polar grid. When the index of the lower radial cut off point is increased the tracked error signal reduces. However, the number of samples to determine the error measurement decreases and the statistical fluctuations begin to dominate the error measurement. The random variation may mask potential signals of interest that are present in $G(u, v; \theta_{(0;\pi)})$. Hence,

it is important to differentiate systematic errors and random variation. Furthermore it is vital to differentiate systematic errors due to the image and the adapted signal processing techniques. In Figure 5, we show how the sources of error in the correlation signal are mitigated using our technique. To test this, we increment the image re-sampling factor and compare the measurement accuracy of nearest-neighbour and linear interpolation for rotations of $H(u, v; \phi_{(0;\pi)})$. Whereby, the random errors are expected to remain constant across the rotation map.

Figure 5 Average error tracking $\bar{\sigma}_\theta$ (y-axis) at reference signal rotation angle ϕ (x-axis), for increases in $s_f = 1, 2, 4, 8$. (a)–(d) nearest-neighbor interpolation, (e)–(h) linear interpolation for $r_j; j = 50$



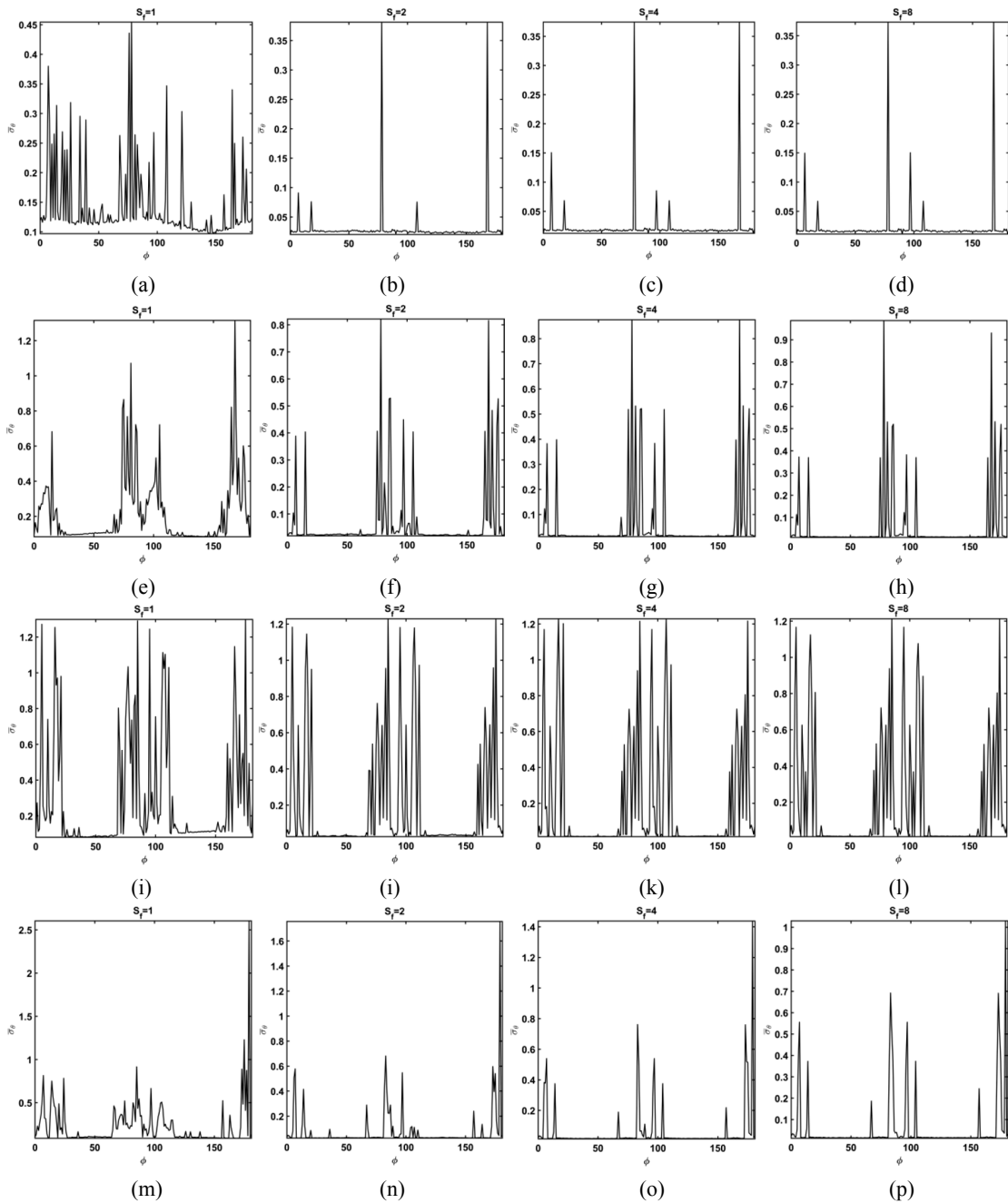
Firstly, for both nearest-neighbour (Figure 5(a)–(d)) and linear interpolation (Figure 5(e)–(h)) the visual similarities between the correlation maps increase as the sampling factor, applied to the test image, increases; The visual similarity described is clearly observed for $s_f = 1, 2$. There is symmetry in the tracked error signal at 90° and the same spurious signals remain. Therefore these spurious signals can be considered independent of the interpolation method. A comparison between the interpolation methods is summarised in Table 1. The error is characterised by a baseline error σ_b , this is equal to the average of σ_θ for each discrete rotation computed between the correlation of $G(u, v; \theta_{(0;\pi)})$ and $H(u, v; \phi_{(0;\pi)})$. It is important to note that each σ_b takes into account the amplitude of the spurious

signals which may be relatively large compared to the statistical fluctuation.

Table 1 Comparison of re-sampled interpolation methods

	<i>Nearest-neighbour</i> σ_b	<i>Linear</i> σ_b	<i>Relative difference</i>	<i>Improvement-factor</i>
$s_f = 1$	0.1239	0.1084	0.0155	–
$s_f = 2$	0.0394	0.0369	0.0025	6.2
$s_f = 4$	0.0332	0.0324	0.0008	3.125
$s_f = 8$	0.0324	0.0321	0.0003	2.6

Figure 6 Average error tracking $\bar{\sigma}_\theta$ (y-axis) at reference signal rotation angle ϕ (x-axis), for $s_f = 1, 2, 4, 8$. From left to right: nearest-neighbor interpolation for $r_j; j = 50$. (a)–(d), (e)–(h), (i)–(l) and (m)–(p) correspond to Figure 3(b)–(e)



There are significant improvements for the nearest-neighbour interpolator by increasing the sampling factor to 2. For the test image in Figure 3(a), the improvement is 6.2: improvement factor denotes the decreasing relative difference, or effective gain, of using nearest neighbour interpolation in comparison to linear interpolation. For the nearest-neighbour method, the relative difference to linear interpolation approaches 1% and for further increases in sampling this reduces to 0.1%.

The comparison between the effects of re-sampling and the two interpolation strategies demonstrates the key steps and advantages of this rotation independent correlation algorithm. The simplicity of using a nearest-neighbour interpolator whilst enhancing rotational displacement measurement, that is comparable to linear interpolation, are the stand out features of this technique. Additional examples of the technique are now presented to reinforce the claims that have been made. With reference to the images in Figure 3(b)–(e), Figure 6 describes their respective correlation maps.

Improvement in the baseline error, σ_b , as compared to linear interpolation, due to increases in the sampling factor are presented in Table 2. We have demonstrated our correlation technique to meet a consistent improvement between interpolation methods for $s_f = 2$. Figure 3(d) contains a high coverage of symmetrical rigid structure and is the exception. The higher proportion of distortion shown in Figure 6(i)–(l) evidently demonstrates systematic errors significantly biasing the baseline error against the random variation across the entire rotational correlation maps. However, the error reduces as the sampling factor increases. This pattern of behaviour is observed in each example.

The proposed technique decomposes the spatial frequency information of the image to form a series of 1D correlation signals. Each correlation's spatial frequency components may also be considered potential key-points. However, these key-points may not be salient or discriminate. Similarly, as discussed in Section 1, region based methods can be thought as operating in the same manor. To compare the achieved measurement accuracy of our technique, we apply SURF, BRISK and ORB detectors to the example images in Figure 3. The error maps of each region based technique quantify the absolute rotational error $|\varepsilon_\theta| = |\theta_A - \theta_R|$, where θ_A and θ_R are the actual and recovered rotation values. Caveat to this comparison is the following condition: region based descriptors are indirectly related to the spatial frequency distribution of the image; this is because search based rules are usually applied to key-point detection and quantification in the spatial domain. Critical features include edges, corners and region statistics. Unless each key-point is inspected individually we take advantage of the fact that these approaches output a cumulative rotation measurement. Using MATLAB, the selected region based algorithms are initialised using defaulted parameters. Critically, the rotation maps obtained from SURF, BRISK and ORB do not produce comparable error signature. This is simply because the key descriptors

of each method are different and larger errors at possibly particular and different rotations may occur. Therefore, the cumulative absolute errors, collated in Table 3, are the discriminant comparable feature of each rotation map.

Table 2 Measurement consistency: re-sampled nearest-neighbour interpolation

<i>Natural structured image Figure 3(b)</i>		
	<i>Nearest-neighbour σ_b</i>	<i>Improvement-factor</i>
$s_f = 1$	0.1435	–
$s_f = 2$	0.0299	4.8
$s_f = 4$	0.023	1.3
$s_f = 8$	0.0221	1.04
<i>Natural structured image Figure 3(c)</i>		
$s_f = 1$	0.214	–
$s_f = 2$	0.0654	3.27
$s_f = 4$	0.023	1.12
$s_f = 8$	0.0221	1.07
<i>Rigid structured image Figure 3(d)</i>		
$s_f = 1$	0.2912	–
$s_f = 2$	0.1977	1.47
$s_f = 4$	0.1854	1.07
$s_f = 8$	0.1807	1.03
<i>Rigid structured image Figure 3(e)</i>		
$s_f = 1$	0.2307	–
$s_f = 2$	0.0771	3
$s_f = 4$	0.0618	1.25
$s_f = 8$	0.0601	1.03

Table 3 Measurement error: selected region based methods: SURF, ORB, BRISK

	<i>Figure 3(a)</i>	<i>Figure 3(b)</i>	<i>Figure 3(c)</i>	<i>Figure 3(d)</i>	<i>Figure 3(e)</i>
<i>SURF</i> $ \bar{\varepsilon}_\theta $	1.559	0.0530	0.0791	0.0347	0.0719
<i>ORB</i> $ \bar{\varepsilon}_\theta $	0.0966	0.0267	0.0346	2.0572	2.0816
<i>BRISK</i> $ \bar{\varepsilon}_\theta $	0.293	2.0695	2.1153	0.0502	0.1012

With reference to the example images Figure 3(a)–(e), the average absolute error of ORB over the rotational range is consistently less than that of SURF and BRISK for the example natural scenes. For the varying image content between natural and rigid structure, our proposed algorithm

consistently provides an error range with $\sim 0.1\%$ of a degree for a sampling factor equal to 2. An exception to the consistency of the error measurement, which may be due to much rigid symmetry, is Figure 3(d). Whereby, the error range variation is 0.1–10% of a degree.

In our preliminary analysis of we have demonstrated that the measurement difference between a nearest neighbour interpolator and a linear interpolator is significantly reduced when the re-sampling factor equals 2. We draw example from the observed baseline errors to specify that small rotation variations towards $\sim 0.1\%$ of a degree can be reliably measured. However, this figure of merit is demonstrated to be dependent on image structure. The authors in Fujisawa and Ikehara (2019) propose a technique based on the Radon transform (Harrison, 1984) and have recorded rotation measurements from popular test images, for example ‘Lena’, and compared with phase correlation and SIFT (Lowe, 2003). The image dependent accuracies are 10% of a degree over a range of 45° and are demonstrated to outperform both phase correlation and SIFT (a similar technique to SURF). In Acciaioli et al. (2018), a small magnitude, $<0.1\%$, DIC technique for in-plane strain measurements is investigated. In Sousa et al. (2018), the authors propose a point cloud data technique to recover rotation measurements, the experimental observed errors of that study are approximately 3% of a degree.

Neglecting contributions to the overall error due to focusing (blur), the error limits of our technique due to optimised sampling and interpolation are comparable to typical DIC system errors that utilise cross correlation methods. A drawback of the technique is that the rotational ambiguity is $\pm 90^\circ$ due to the 180° viewing angle range of the autocorrelation and the two-fold symmetry of the polar spatial frequency space. Two points to consider that may improve the measurement sensitivity are taking the edge image and approximating sinc convolution with higher-order interpolators: such as cubic and spline interpolation. However, if features of interest are not at high spatial frequencies the edge image may not adequately represent the signal. In addition the correlation peak may be unnecessarily over sampled since the shape of the correlations curve is parabolic. This may not improve the situation.

5 Conclusions

In this paper, we have presented a series of results that emphasise the rotational measurement accuracy of a non-uniformly sampled correlation technique. This technique incorporates a modified coordinate transform and the simple nearest-neighbour interpolator. Our example data set consistently demonstrates an overall rotation error of 0.1%. Systematic errors imposed by the interpolation method and initial image quality are reduced, such that spurious signal peaks may be analysed with a higher degree of confidence and localised to individual spatial frequency components. In turn, each image autocorrelation identifies polar spatial frequency components with high S/N. It is

shown that error locations across a correlation rotation map are symmetrical about 90° . Consequently, this increases the rotational ambiguity to $\pm 90^\circ$. An important drawback of the technique is a requirement to meet the sampling condition per radial unit. At the expense of image width or height, this is achieved by linearly increasing the radial sampling rate as the distance from the origin of the polar grid increases. Hence, the computational complexity is dominated by satisfying the sampling condition at each radii on the polar grid. This complexity increases due to scaling from rotating the reference and target images. Furthermore, the correlations spatial bandwidth may be limited by additive noise (photon shot noise, read out noise, flicker noise), low contrast images and the imaging devices’ aperture. Whereby, the lower radial cut off point (r_j) of a correlation signal varies with noise power and location of interesting polar spatial frequency components.

We believe that due to a broad correlation spatial bandwidth and high rotation measurement sensitivity, this technique would be of great value in surface deformation analysis. In particularly, when applications are data-driven and distorted by small scale variation and when surface texture patterns are discontinuous. Work is currently underway to investigate shape deformation measurement tracking. Further research could include developing modifications to the technique and integrating the application methodology to form hybrid machine learned registration models. For applications driven by high measurement sensitivity, this may potentially reduce the searchable regions in image frames to register rotations and provide post process accurate rotation measurement estimates.

Disclosures

There are no conflicts of interest.

Acknowledgements

This work was supported by the Engineering and Physical Sciences Research Council, award number: 1510476. When the work was carried out, both authors were with Faculty of Engineering, University of Nottingham, UK.

References

- Acciaioli, A., Lionello, G. and Baleani, M. (2018) ‘Experimentally achievable accuracy using a digital image correlation technique in measuring small-magnitude ($<0.1\%$)’, *Homogeneous Strain Fields. Materials*, Vol. 11, p.751 [doi:10.3390/ma11050751].
- Bay, H. et al. (2008) ‘Speeded-Up Robust Features (SURF)’, *Comput. Vis. Image Underst.*, Vol. 110, pp.346–359 [doi:10.1016/j.cviu.2007.09.014].
- Casasent, D. and Psaltis, D. (1976) ‘Position, rotation, and scale invariant optical correlation’, *Applied Optics*, Vol. 15, No. 7, pp.1795–1799 [doi:10.1364/AO.15.001795].

- Charrett, T. and Tatam, R. (2019) ‘Performance and analysis of feature tracking approaches in laser speckle instrumentation’, *Sensors*, Basel, Switzerland, p.19 [doi:10.3390/s19102389].
- Deng, J. *et al.* (2009) ‘ImageNet: A large-scale hierarchical image database’, *2009 IEEE Conference on Computer Vision and Pattern Recognition*, Miami, FL, pp.248–255 [doi:10.1109/CVPR.2009.5206848].
- Fujisawa, T. and Ikehara, M. (2019) ‘High-accuracy image rotation and scale estimation using radon transform and sub-pixel shift estimation’, in *IEEE Access*, Vol. 7, pp.22719–22728 [doi:10.1109/ICASSP.2019.8682679].
- Harrison, B.H. (1984) ‘III the radon transform and its applications’, *In Prog. Opt.*, Vol. 21, No. C, pp.217–286.
- Kumar, B.V., Dickey, F.M. and DeLaurentis, J.M. (1992) ‘Correlation filters minimizing peak location errors’, *J. Optical. Soc. America A*, Vol. 9, pp.678–682 [doi:10.1364/JOSAA.9.000678].
- Lee, W., Sim, D. and Oh, S.-J. (2021) ‘A CNN-based high-accuracy registration for remote sensing images’, *Remote Sens*, Vol. 13, No. 1482 [doi.org/10.3390/rs13081482].
- Leutenegger, S. *et al.* (2011) ‘BRISK: Binary Robust invariant scalable keypoints’, *2011 International Conference on Computer Vision*, pp.2548–555 [doi:10.1109/ICCV.2011.6126542].
- Lowe, D.G. (2003) ‘Distinctive image features from scale-invariant keypoints’, *Int. J. Computer Vision*, Vol. 20, No. 01, pp.91–110.
- O’Mahony, N. *et al.* (2019) ‘Deep learning vs. traditional computer vision’, in *Advances in Computer Vision Proceedings of the 2019 Computer Vision Conference (CVC)*, Springer Nature Switzerland AG, pp.128–144 [doi.org/10.48550/arXiv.1910.13796].
- Rasmy, L., Sebari, I. and Ettarid, M. (2021) ‘Automatic sub-pixel co-registration of remote sensing images using phase correlation and Harris detector’, *Remote Sens*, Vol. 13, No. 2314, pp.1–19 [doi.org/10.3390/rs13122314].
- Reddy, B.S. and Chatterji, B.N. (1996) ‘An FFT-based technique for translation, rotation, and scale-invariant image registration’, *IEEE Trans. Imag. Process.*, Vol. 5, pp.1266–1271 [doi: 10.1109/83.506761].
- Rublee, E. *et al.* (2011) ‘ORB: An efficient alternative to SIFT or SURF’, *2011 International Conference on Computer Vision*, pp.2564–2571 [doi:10.1109/ICCV.2011.6126544].
- Sarvaiya, J.N., Patnaik, S. and Kothari, K. (2012) ‘Image registration using log polar transform and phase correlation to recover higher scale’, *J. Pattern. Recog. Res.*, Vol. 7, pp.90–105 [doi:10.13176/11.355].
- Schreier, H., Orteu, J.J. and Sutton, M.A. (2009) ‘Image correlation for shape, motion and deformation measurements: basic concepts, theory and applications’, *Digital Image Correlation (DIC)*, Springer, pp.81–108 [doi:10.1007/978-0-387-78747-3].
- Sousa, P.J., Barros, F., Tavares, P.J. and Moreira, P.M.G.P. (2018) ‘Digital image correlation displacement measurement of a rotating RC helicopter blade’, *Engineering Failure Analysis*, Vol. 90, pp.371–379 [doi:10.1016/j.engfailanal.2018.04.005].
- Sousa, P.J., Tavares, J.M.R., Tavares, P.J. and Moreira, P.M. (2018) ‘Correction of rigid body motion in deformation measurement of rotating objects’, *Measurement*, Vol. 129, pp.436–444 [doi:10.1016/J.MEASUREMENT.2018.07.049].
- Titkov, V.V. and Panin, S.V. (2019) ‘Measurement affecting errors in digital image correlation’, *IOP Conf. Ser.: Mater. Sci. Eng.*, Vol. 511, p.012018 [doi.org/10.1088/1757-899X/511/1/012018].
- Tong, X. *et al.* (2019) ‘Image registration with fourier-based image correlation: a comprehensive review of developments and applications’, in *IEEE Journal of Selected Topics in Applied Earth Observations and Remote Sensing*, Vol. 12, No. 10, pp.4062–4081 [doi: 10.1109/JSTARS.2019.2937690].
- Villena-Martinez *et al.* (2021) ‘When deep learning meets data alignment: a review on deep registration networks (DRNs)’, *Appl. Sci.*, Vol. 10, p.7524 [doi.org/10.3390/app10217524].
- Wolberg, G. and Zokai, S. (2000) ‘Robust image registration using log-polar transform’, *Proceedings 2000 Int. Conf. Image Process (Cat. No.00CH37101)*, Vancouver, BC, Canada, Vol. 1, pp.493–496 [doi:10.1109/ICIP.2000.901003].
- Xiang, C. *et al.* (2021) ‘Deep learning in medical image registration’, *Prog. Biomed. Eng.*, Vol. 3, No. 1, pp.1–29 [doi.org/10.1088/2516-1091/abd37c].

Appendix

The 2D Fourier transform

$$H(u, v) = \int_{-\infty}^{\infty} \int_{-\infty}^{\infty} h(x, y) e^{-j2\pi(ux+vy)} dx dy \quad (A1)$$

can be viewed as two successive 1D transforms. Hence we can re-write Equation (A1) as

$$H(u, v) = \int_{-\infty}^{\infty} e^{-j2\pi vy} \left[\int_{-\infty}^{\infty} h(x, y) e^{-j2\pi ux} dx \right] dy \quad (A2)$$

Consider two functions where one is a rotated and translated replica of the other

$$h(x, y) = g(x \cos \theta_0 + y \sin \theta_0 - x_0, -x \sin \theta_0 + y \cos \theta_0 - y_0). \quad (A3)$$

From the Fourier translation and rotation property Equation (A3) becomes

$$H(u, v) = G(u \cos \theta_0 + v \sin \theta_0, -u \sin \theta_0 + v \cos \theta_0) e^{-j2\pi(x_0 u + y_0 v)}, \quad (A4)$$

whereby all points in frequency space are first rotated and then shifted in phase by the translation. An examination of Equation (A4) reveals that the magnitude of $H(u, v)$ is invariant to phase displacement. For $\hat{u} = u \cos \theta_0 + v \sin \theta_0$ and $\hat{v} = -u \sin \theta_0 + v \cos \theta_0$, the polar coordinate conversion of \hat{u} and \hat{v} is

$$H(r, \theta) = G(r, \theta \pm \theta_0). \quad (A5)$$

Hence, each radial component r_j , sampled by $\theta_{i(0:2\pi)}$, returns a series of 1D polar frequency coordinates. A rotation about the origin on a polar grid transformed back to a Cartesian grid corresponds to a linear horizontal translation. The Fourier transform in Equation (A5) reveals a phase relationship that is deduced by applying a correlation to reveal a peak location at $\delta(r, \theta \pm \Delta\theta)$. Increasing the radial or the angular increment changes the grid space of the annular region. This adjusts the sampling rate and therefore yields a degree of freedom to manipulate nonlinear grid spacing.